A General Analytical Formulation for the Motional Parameters of Piezoelectric MEMS Resonators

Jonathan M. Puder, *Member, IEEE*, Jeffrey S. Pulskamp, Ryan Q. Rudy,
Ronald G. Polcawich, *Senior Member, IEEE*, and Sunil A. Bhave, *Senior Member, IEEE*

***Abstract*— This paper reports on a general analytical expression for the motional resistance (R_m) of an arbitrary mode in a piezoelectric microelectromechanical system resonator with parallel plate electrode geometry. After applying simplifying assumptions and using analytical modes shapes, expressions for the R_m of modes with out-of-plane flexure as the primary displacement are presented. These modes include free–free transverse beam flexure (TBF), unclamped disk flexure resonators (DFRs), and antisymmetric A_0 Lamb modes. For verification, R_m is extracted from resonators fabricated in a lead zirconate titanate on silicon process. Predicted R_m of TBF and DFR modes is validated using on-wafer extracted e_{31} constants, analytical modal properties, and independently measured material properties.**

***Index Terms*— Disk resonator, lead zirconate titanate (PZT), microelectromechanical system (MEMS) resonator.**

I. Introduction

PIEZOELECTRICALLY transduced contour-mode radio frequency (RF) microelectromechanical system (MEMS) resonator technology offers a solution to demands for highly integratable, low-loss band-select filters in an increasingly contested and dynamic frequency space. Lithographic design of frequency allows for monolithic integration of multiple frequencies on a single chip. In addition, high-coupling piezoelectric materials enable device design for direct interface with 50-Ω terminated networks, eliminating the need for bulky matching components [1].

Despite the promise of contour piezoelectric MEMS resonator technology, challenges still exist toward a fully realized commercial product or implementation in military systems. A significant challenge is the spurious mode ("spurs") problem. Spurious modes allow signals to pass through filters at undesired frequencies and degrade response by generating passband ripples and affecting the group delay. Part of the reason spurious modes remain problematic is the lack of a general framework to model the effect of an arbitrary mode on the filter passband of a resonator with arbitrary geometry. Models for specific modes with specific electrode shapes exist, but are not generalized to model any mode [2]–[5]. Due to the lack of comprehensive and quantitative predictive models, current approaches to design generally consider a single-target mode, and spurs are generally identified and analyzed after fabrication and testing. This is due to the reliance on finite-element analysis (FEA) to model the complex 3-D geometries involved. These full 3-D simulations often take at a minimum several hours to complete. With a simplified analytical model depending less upon a full computational solution, design cycles times could be greatly decreased.

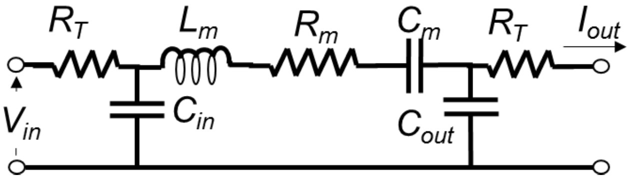

Fig. 1. Two-port mBVD circuit model for piezoelectrically transduced RF MEMs resonators.

Accordingly, this paper will present general analytical expressions for the modified Butterworth van Dyke (mBVD) motional parameters Fig. 1 and effective electromechanical coupling factor k^2_{eff} of an arbitrary mode in devices with parallel plate electrode configurations [6]. Contour-mode resonators of this topology tend to exist below several hundred mehahertz. Demanding defense applications, such as SINGCARS [7] and HAVE QUICK [8], utilize these HF to low-UHF frequencies. The mBVD parameters derived are the motional resistance R_m, the motional inductance L_m, and the motional capacitance C_m. Although devices in this paper are PZT based and two-port, the method applies to non-PZT based one-port resonators as well.

Though this model and the modes analyzed share elements with the recently published textbook [5], there are several key differences. This framework is generalized to model an arbitrary mode, displacement profile, and/or material stack with parallel plate electrodes, and presents easily applicable general expressions for the R_m and k^2_{eff}. The closed-form general solution allows designers to, for example, quickly investigate the effect of the piezoelectric crystallographic axes orientation upon device performance or rapidly identify high-coupling modes. Mode shapes from FEA may also be used in the expression for more accurate models of complex topologies. In addition, closed-form expressions for the true displacement (and therefore velocity) and the true charge accumulated (and therefore current output) on the output electrode are presented,

Manuscript received June 20, 2017; accepted January 9, 2018. Date of publication January 12, 2018; date of current version March 1, 2018. *(Corresponding author: Jonathan M. Puder.)*

J. M. Puder is with the Sibley School of Mechanical and Aerospace Engineering, Cornell University, Ithaca, NY 14850 USA, and also with the General Technical Services, U.S. Army Research Laboratory, Adelphi, MD 20783 USA (e-mail: jmp378@cornell.edu).

J. S. Pulskamp, R. Q. Rudy, and R. G. Polcawich are with the USA Sensors and Electron Devices Directorate, U.S. Army Research Laboratory, Adelphi, MD 20783 USA.

S. A. Bhave is with the Department of Electrical Engineering, Purdue University, West Lafayette, IN 47907 USA.

Digital Object Identifier 10.1109/TUFFC.2018.2793099

making this modeling framework useful in a variety of resonant and nonresonant systems outside of filtering purposes, such as ultrasonic motors, transformers, strain sensors, and actuators. However, these applications are beyond the scope of this paper.

Resonant modes which feature out-of-plane flexure as the main form of displacement will be analyzed to illustrate the usefulness of this model. Closed-form expression of mBVD parameters for the analyzed flexure modes do not exist, even though they often show up as spurious modes, and early research explored utilizing such modes [9]–[12]. Modes analyzed will include transverse beam flexure (TBF), the (1,1) disk flexure resonator (DFR) mode, and the antisymmetric A_0 Lamb mode, a plate flexure mode. At frequencies below several hundred megahertz, TBF modes are considered spurious modes to the commonly utilized length extension (LE) modes. For DFR modes, recent designs have demonstrated subdecibel insertion loss with direct 50-Ω termination at 20 MHz, and therefore, it is desirable to have models for such high-performance modes [1], [13]–[15]. A_0 Lamb modes are considered a spurious to the S_0 modes commonly utilized in higher frequency resonator designs [16]–[19].

TBF and DFR mBVD predictions are validated in a lead zirconate titanate (PZT)-on-silicon process, which has been used to demonstrate high-performance resonators at frequencies below 500 MHz [14], [15], [20].

The remainder of this paper will proceed as follows. Section II will present a general expression R_m and k_{eff}^2 and expressions for the R_m of specific modes based on analytical mode shapes. Section III will provide an overview of the fabrication process. Section IV will discuss experimental validation for DFR and TBF resonant modes. Section V will conclude this paper.

II. MODELING

The fabricated resonant system is modeled as a forced lumped mass-spring system using the principles of modal analysis. This is achieved by comparing the work done by the piezoelectric layer in the continuous system to the work done by the modal force in the lumped system. These expressions use modal strains derived from unity normalized modes shapes. A real displacement, derived from Hooke's law and normalized mode shape, is then predicted. This real displacement is in turn used to predict the real strain. The piezoelectric constitutive equation is then used to find the charge on the output port. Taking a time derivative returns the output current, which is used to derive the motional resistance. The motional capacitance and inductance are derived from the definition of the quality factor.

The following sections will proceed as follows. Section II-A will present a general expression for the current out of the resonator and R_m, and Section II-B will present a form that that applies only to materials with piezoelectric coefficients similar to those of PZT and aluminum nitride. Section II-C will derive R_m expressions for free–free beam flexure modes with several common electrode patterns, and a comparison to LE modes will be performed. Section II-D will address the analytical R_m expression for the (1,1) mode of disk flexure. Section II-E will be concerned with A_0 Lamb wave resonators, and briefly touch on some of the complexities required to model such modes. Finally, Section II-F will discuss the results and provides insights into generally designing resonators for low R_m and high k_{eff}^2.

A. Generalized Current and Motional Resistance

The principles of modal analysis are used to convert the continuous acoustic system into a discrete damped mass-spring system. Two important concepts from modal analysis are critical to this conversion. First, for systems in which mechanical modes have weak acoustic coupling, each mode may be considered individually. The generalized frequency-dependent motion is then a superposition of the natural modes [21]. This allows for the analysis of a single mode independent of all others. The second important concept is that all points in a given mode vibrate with the same frequency and phase. Accordingly, the total potential and kinetic energies for a lossless system are sinusoidally varying quantities, akin to a discrete mass-spring system. Therefore, discrete modal stiffness and modal masses may be defined relative to a point on the continuous system, called the modal displacement [22]. Expressions for the total elastic potential and kinetic energies without damping are used in the Lagrangian, from which the equation for the undamped simple harmonic oscillator with modal mass m_m and modal stiffness k_m are derived relative to the modal displacement [23].

From modal analysis, if one mode is considered, its displacement may be written as a product of the time dependent and spatially dependent components of the displacement. The real displacement of a single mode may be expressed as

$$u = \delta u_n u_t \tag{1}$$

where u_n is the unity normalized mode shape, δ is the zero-frequency displacement amplitude as well as the modal displacement of the lumped parameter spring, and u_t is the frequency response given by

$$u_t(t) = \frac{e^{j\omega t}}{\left[\left(1-\left(\frac{\omega}{\omega_n}\right)^2\right)+\frac{\omega}{\omega_n Q_m}\right]} \tag{2}$$

where ω is the frequency of excitation, ω_n is the natural frequency, and Q_m is the mechanical quality factor.

The transduction of electrical energy into mechanical energy may be modeled as a modal force F_m on the system. To find the modal force, the energy of the real system is compared to the energy stored in the modal spring. The elastic strain energy is given by

$$\text{PE} = \frac{1}{2}\int_V \boldsymbol{T}\cdot\boldsymbol{S}dV \tag{3}$$

where T and S are the 6-D condensed vector representations of stress and strain, respectively, in Voigt's notation, and V is the volume of the resonator. Next, the stress-charge form of the indirect effect piezoelectric constitutive equation is used

$$\boldsymbol{T} = \boldsymbol{c}_E\cdot\boldsymbol{S} - \boldsymbol{e}^t\cdot\boldsymbol{E} \tag{4}$$

where c_E is the matrix of stiffness coefficients at constant (zero) electric field, e is the matrix of piezoelectric constants, and E is the electric field. Energy already present in the system is accounted for by the stiffness-strain term, and is ignored since the concern is with additional energy transduced into resonator from the modal force/applied piezoelectric stress. The piezoelectric is assumed to have low to moderate coupling.

For all resonators modeled from hereon, the modal displacement is the maximum displacement of the acoustic system, as implied in (1). To find the modal force, the system is analyzed under a quasi-static condition [i.e., $\omega \approx 0$, so $u = \delta u_n$ in (2)], and so only the spatial component is considered. The work done by the modal force for the discrete system and applied stress for the continuous system are equated using (3)

$$\frac{1}{2}F_m\delta = \frac{1}{2}k_m\delta^2 = \frac{1}{2}\int_{V_{\text{in}}} \boldsymbol{T}_p \cdot \delta\boldsymbol{S}_n dV \tag{5}$$

where F_m is the modal force, k_m is the modal stiffness [22], T_p is the applied piezoelectric stress [i.e., the right-most term from (4)], and S_n is the strain of the unity normalized mode shape, and therefore, δS_n is the quasi-static real strain. Since the piezoelectric stress only exists in the parts of the resonator where the piezoelectric sees applied electric field, the integral is zero everywhere else. Therefore, the modal force may be expressed as

$$F_m = k_m\delta = -\int_{V_{\text{in}}} \boldsymbol{e}^t \cdot \boldsymbol{E}_{\text{app}} \cdot \boldsymbol{S}_n dV \tag{6}$$

where E_{app} is the applied electric field. With parallel plate electrodes whose lateral dimensions are much larger than the distance between them assumed

$$\mathbf{E}_{\text{app}} = \begin{bmatrix} 0 & 0 & \dfrac{\phi_{\text{in}}}{t_p} \end{bmatrix}^t \tag{7}$$

where ϕ_{in} is the applied voltage on the input port, and t_p is the thickness of the piezoelectric layer. The corresponding quasi-static displacement is

$$\delta = \frac{F_m}{k_m} = -\frac{\phi_{\text{in}} \int_{A_{\text{in}}} e^t \cdot \overline{\boldsymbol{S}}_n dA}{k_m} \tag{8}$$

where $\overline{S}_n$ is the strain of the unity normalized mode averaged through the piezoelectric layer thickness. Note that by placing (7) into (6), the e matrix of (6) is reduced to a 6-D vector since the electric field only exists in a single direction. From (8) onward, e is a vector consisting of the third row of the e matrix due to an assumed three-direction electric field, except for in (10).

Now, the frequency dependent real average strain may be expressed as

$$\overline{\boldsymbol{S}} = \delta\overline{\boldsymbol{S}}_n u_t. \tag{9}$$

And used in the stress-charge form of the direct effect piezoelectric constitutive equation on the output port of the resonator

$$\boldsymbol{D} = \boldsymbol{e} \cdot \boldsymbol{S} + \boldsymbol{\varepsilon}_s \cdot \boldsymbol{E} \tag{10}$$

where D is the electric displacement, and ε_s is the electric permittivity measured at constant strain. The second term on the right-hand side accounts for electrical energy already present on the output port, and is thus ignored, since the concern is with additional charge created by the induced strain. The electrical energy stored in the piezoelectric film from the induced strain is compared to the energy stored in a capacitor

$$\frac{1}{2}\int_V \boldsymbol{D}_p \cdot \boldsymbol{E}_{\text{out}} dV = \frac{1}{2}Q_{\text{out}}\phi_{\text{out}} \tag{11}$$

where D_p is the induced electric displacement in the piezoelectric layer, E_{out} is the electric field of the output port capacitor created by the electric displacement, Q_{out} is the charge on the output capacitor, and ϕ_{out} is the magnitude of the potential induced on the output capacitor. Substituting (10) into (11) with the second term omitted and the and using true average strain, as well as the parallel plate assumption (7)

$$Q_{\text{out}} = \int_{A_{\text{out}}} \boldsymbol{e} \cdot \delta\overline{\boldsymbol{S}}_n dA u_t. \tag{12}$$

Now, substituting (8) into (12)

$$Q_{\text{out}} = -\frac{\phi_{\text{in}}}{k_m}\int_{A_{\text{in}}} \boldsymbol{e} \cdot \overline{\boldsymbol{S}}_n dA \int_{A_{\text{out}}} e \cdot \overline{\boldsymbol{S}}_n dA u_t. \tag{13}$$

This is the quasi-static charge developed on the output port. The time- and frequency-dependent charge is obtained by multiplying (13) by (2). Using $\omega = \omega_n$ in this product (setting the frequency to the natural frequency) and differentiating with respect to time returns current out of the resonator at resonance

$$|I_{\text{out}}| = -\frac{\phi_{\text{in}} Q_m \omega_n}{k_m}\int_{A_{\text{in}}} \boldsymbol{e} \cdot \overline{\boldsymbol{S}}_n dA \int_{A_{\text{out}}} e \cdot \overline{\boldsymbol{S}}_n dA u_t. \tag{14}$$

Reorganizing this and taking the absolute returns the magnitude of R_m

$$R_m = \frac{k_m}{Q_m \omega_n \left| \int_{A_{\text{in}}} \boldsymbol{e} \cdot \overline{\boldsymbol{S}}_n dA \int_{A_{\text{out}}} e \cdot \overline{\boldsymbol{S}}_n dA \right|}. \tag{15}$$

This is the most general expression for R_m, and the expression is valid for any material stack with parallel plate electrodes and negligible fringing field effects.

For each of the following modes analyzed, the modal stiffness and natural frequency must be derived, e constants must be input, and Q_m must be assumed or extracted from measured data. Equation (15) is also applicable to one-port resonators, with the primary difference being the transduction of strain-to-charge and charge-to-strain occurring on the same capacitor. After inserting a value for Q_m, the remaining mBVD motional parameters may be derived using the definition of Q

$$L_m = \frac{m_m}{\left| \int_{A_{\text{in}}} \boldsymbol{e} \cdot \overline{\boldsymbol{S}}_n dA \int_{A_{\text{out}}} e \cdot \overline{\boldsymbol{S}}_n dA \right|} \tag{16}$$

$$C_m = \frac{\left| \int_{A_{\text{in}}} \boldsymbol{e} \cdot \overline{\boldsymbol{S}}_n dA \int_{A_{\text{out}}} e \cdot \overline{\boldsymbol{S}}_n dA \right|}{k_m} \tag{17}$$

where m_m is the modal mass. When (17) is placed in the equation for k_{eff}^2 (18), it gives a convenient expression to predict coupling [24]

$$k_{\text{eff}}^2 = \frac{1}{\frac{C_0}{C_m} + 1} = \frac{1}{\frac{k_m C_0}{\left|\int_{A_{\text{in}}} \boldsymbol{e}\cdot\overline{\boldsymbol{S}}_n dA \int_{A_{\text{out}}} e\cdot\overline{\boldsymbol{S}}_n dA\right|} + 1} \tag{18}$$

where C_0 is the shunt capacitance for a one-port resonator, or the equivalent capacitance of C_{in} and C_{out} (Fig. 1) when placed in series to create an equivalent one-port resonator (Fig. 1) as in [13]. For maximum coupling, the denominator should be minimized. k_{eff}^2 is a measure of how much mechanical energy is transduced from electrical energy, or *vice versa*. This definition will be important later when design for optimal performance is discussed. If the quality factor is known, it is trivial to obtain the figure of merit, $k_{\text{eff}}^2 \cdot Q_m/(1 - k_{\text{eff}}^2)$.

B. Simplification for PZT and Aluminum Nitride

For PZT and aluminum nitride, only the e_{31}, e_{32}, and e_{33} piezoelectric constants of the e matrix can contribute stress from a three-direction electric field. In addition, throughout the rest of this paper, the electrodes will be assumed symmetric with respect to the resonator yz midplane defined in Fig. 2. This simplifies (15) to

$$R_m = \frac{k_m}{Q_m \omega_n \left(\int_{A_{\text{el}}} (e_{31}\overline{S}_{n_1} + e_{32}\overline{S}_{n_2} + e_{33}\overline{S}_{n_3}) dA\right)^2}. \tag{19}$$

C. Free–Free Transverse Beam Flexure Modal Properties and Motional Resistance

TBF modes are generally considered spurious to resonators designed for LE [25], [26]. TBF and LE modes may be considered 1-D modes if their length is much greater than their width and thickness. 1-D modes have a single significant component of stress or strain. Typical electrode designs for LE resonators with nonsymmetric material stacks unavoidably transduce energy into TBF. This is because TBF and LE both have their primary stresses in plane, although TBF modes primarily displace out of plane, while LE modes displace in plane.

Analytical expressions for the natural frequency and mode shape of a 1-D free–free transverse flexure beam from the Euler–Bernoulli theorem are well known and are given by [27]

$$u_n(i,x) = \frac{1}{2}\left(\cosh\left(\frac{\lambda_i x}{L}\right) + \cos\left(\frac{\lambda_i x}{L}\right) - \sigma_i\left(\sinh\left(\frac{\lambda_i x}{L}\right) + \sin\left(\frac{\lambda_{ix}}{L}\right)\right)\right) \tag{20}$$

$$\omega_n = \frac{\lambda_i^2}{L^2}\sqrt{\frac{Y_c I}{\rho_c w_{\text{tot}} t_{\text{tot}}}}. \tag{21}$$

The modal mass and stiffness are calculated via the method of [22] and are given by

$$m_m = \frac{m_{\text{tot}}}{4} \tag{22}$$

$$k_m = \frac{Y_c I \lambda_i^4}{4L^3}. \tag{23}$$

In (20)–(23), λ_i and σ_i are frequency parameters, L is length of the beam, I is the second moment of area about the neutral axis, Y_c and ρ_c are the composite elastic modulus and density [28], w_{tot} and t_{tot} are the total widths and thicknesses, respectively, m_{tot} is the total mass, and i is the harmonic. σ and λ must be analytically calculated; tabulated values are available in [27].

Since the beam has only one relevant direction of strain, (19) becomes

$$R_{m_i} = \frac{\sqrt{Y_c I \rho_c w_{\text{tot}} t_{\text{tot}}}}{4LQ_m\left[e_{31} h \int_L \frac{d^2 u_n}{dx^2} w_{\text{el}}(x) dx\right]^2} \tag{24}$$

where h is the distance from the neutral axis to the midplane of the piezoelectric material (Fig. 1).

1) Full-Length, Half-Width Electrodes: A commonly used electrode pattern for LE resonators is two rectangles approximately half the width of the resonator and spanning nearly the full length [Fig. 3(a)] [2], [29]. For the case where i is even, the integral in (24) is 0. For the case of i being odd, then (24) reduces to

$$R_{m_i} = \frac{L\sqrt{Y_c \rho_c I t_{\text{tot}} w_{\text{tot}}}}{4Q_m\left[w_{\text{el}} e_{31} \sigma_i h\left(\cosh\left(\frac{\lambda_i x_1}{L}\right) + \cos\left(\frac{\lambda_i x_1}{L}\right)\right)\right]^2} \tag{25}$$

where x_1 is the x coordinate of the start of the electrode (Fig. 2). In the case where the electrodes span the full length and half the width

$$R_{m_i} = \frac{L\sqrt{Y_c \rho_c I t_{\text{tot}}}}{4Q_m w_{\text{tot}}^{3/2}[e_{31} h \sigma_i]^2}. \tag{26}$$

It is interesting to note that the analytical model predicts motional resistance of TBF is directly proportional to the length of the resonator, and constant across harmonics, since the parameter σ_i is approximately one, and λ_i drops from (26). Due to this constant scaling across harmonic, spurious TBF modes may be problematic in resonator design for LE resonators across a wide range of frequencies. This expression also suggests it may be possible to fabricate low R_m resonators at high frequencies as long as Euler–Bernoulli assumptions are not violated.

2) Alternating Electrodes: To optimally excite a particular harmonic of the 1-D beam flexure, all locations where the strain is of the same sign should be covered by the electrode belonging to one port [11], [13]. To optimally pick off the signal from the harmonic, the electrodes of the other port should cover the parts of the resonator for which the strain is of the opposite sign. This corresponds to a series of rectangles for TBF modes, as seen from Fig. 3(b).

Once again using (24) and numerically evaluating the integral for even order harmonics, the motional resistance is approximately

$$R_{m_i} \approx \frac{L t_{\text{tot}}\sqrt{Y_c \rho_c I / A_{yz}}}{Q_m w_{\text{tot}}[e_{31}\sigma_i h[4 + \sqrt{2}(i-1)]]^2} \tag{27}$$

where the $\sqrt{2}$ is approximated from numerical evaluation of contribution of terms from (20) to the strain. It is important to note that (27) is only valid for the mode that is being

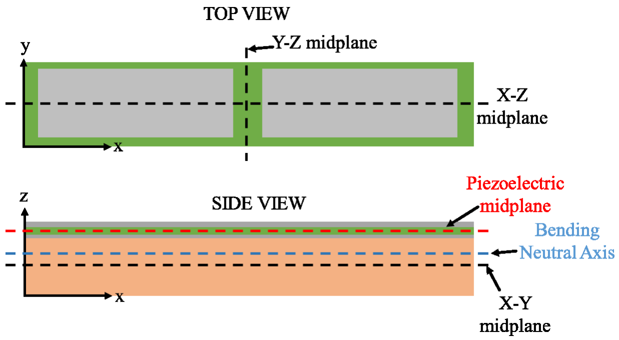

Fig. 2. Definitions of coordinate systems and planes. The green layer is the piezoelectric material.

optimally excited, and would fail to describe different harmonics with the same electrode pattern. This is in contrast to (26) which is valid for all harmonics using a single-electrode design. Interestingly, this expression states that R_m is proportional to a quadratic function of harmonic, i^2. Comparing this to similar electrode designs for LE [3], the TBF motional resistance scales more favorably with harmonic. The LE modes scale as $1/n$, where n is the harmonic number.

3) Comparison to Length Extension for Full-Length, Half-Width Case: A general expression for the LE R_m of full-length, half-width electrodes has been derived using a similar method as in Sections II-C.1 and II-C.2. This expression agrees with that presented in [2]

$$R_m = \frac{n\pi t_{\mathrm{tot}}\sqrt{Y_c\rho_c}}{2Q_m e_{31}^2 w_{\mathrm{tot}}}. \tag{28}$$

Equation (28) reveals that for this electrode pattern, LE modes scale with harmonic, but not length, whereas TFB modes scale with length, but not harmonic. Taking the ratio of LE and TBF R_m

$$\frac{R_{m_{\mathrm{LE}}}}{R_{m_{\mathrm{TBF}}}} = \frac{2n\pi h^2\sigma_i^2}{L_F}\sqrt{\frac{t_{\mathrm{tot}}w_{\mathrm{tot}}}{I}} \approx 4\sqrt{3}\frac{n\pi h^2}{t_{\mathrm{tot}}L_F} \tag{29}$$

where L_F is the length of the flexure beam. This equation is approximate, as the parameter σ_i is approximately 1 across harmonics, and the neutral axis is assumed to be at nearly the same location as the geometric xy midplane (Fig. 2). This suggests that for a single resonator with TBF as a spurious mode, for the LE R_m to be much lower than TBF R_m, the length should be large, the LE mode should be a low harmonic, and/or the devices should be made very thin. Large length and low harmonic correspond to low frequency for LE beams. If considering two different beams, one designed for LE and one designed for TBF, to have comparable R_m to the LE resonator, the TBF resonator must have low length (higher frequency), and be thicker.

In addition, for low TBF R_m, the piezoelectric layer should be far from the neutral axis for h to be as large as possible. For material stacks symmetric about the xy midplane (Fig. 2), the neutral axis coincides with the xy midplane, and the motional resistance is infinite. If TBF is considered a spur, it would be desirable to have this effect.

D. Unclamped Disk Flexure Modal Properties and Motional Resistance

Recent alternative designs at lower frequencies have taken advantage of flexure modes in circular plates [13], [14]. Specifically, the (1,1) disk flexure mode displayed subdecibel insertion loss at 20 MHz. In disk flexure modes, the primary displacements are out of plane, with characteristic nodal circles and diameters defining the mode. Stresses and strains are normal and primarily in plane. In contrast to TBF, DFRs have primary stresses in two orthogonal directions. Due to the demonstrated high performance of the (1,1) mode of disk flexure, a closed-form expression for the motional resistance is desirable to analyze the dependence of resonator performance on geometric and material properties.

Annular disks in flexural modes of vibration have displacements generally described by [30]

$$u(r,\theta) = [AJ_p(kr) + BY_p(kr) + CI_p(kr) + DK_p(kr)]\cos(p\theta) \tag{30}$$

and natural frequency is given by

$$\omega_{n_{pq}} = \frac{\lambda_{pq}^2 t_{\mathrm{tot}}}{R^2}\sqrt{\frac{Y_c}{12\rho_c(1-\nu^2)}} \tag{31}$$

where p and q are the number of nodal diameters and circles, respectively, λ_{pq} is a frequency constant, R is the outer radius of the disk, r abd θ are the coordinates, J and Y are ordinary Bessel functions of the first and second kind, respectively, I and K are modified Bessel functions of the first and second king, respectively, A, B, C and D are amplitudes, and υ is Poisson's ratio. Tabulated values of λ are given in [30]. The modal mass and spring may be calculated via the method of [22]. Amplitudes A, B, C, and D are determined by boundary conditions, which may be found in [31] for disks and rings. For unclamped disks, $B = D = 0$. The ratio of A and C may be determined by the moment boundary conditions and υ, and must be computationally calculated. Since the maximum of (30) is not guaranteed to be 1, a unity normalization constant is introduced $|u_{\max}|$, which must be numerically determined. The (1,1) mode shape is now

$$u_{n_{11}} = [AJ_1(kr) + CI_1(kr)]\frac{\cos(\theta)}{|u_{\max}|}. \tag{32}$$

Since the three-direction strain is ignored for plates, the integral of (19) turns into

$$h\int_{A_{\mathrm{el}}} -e_{31}\frac{\partial^2 u_n}{\partial r^2} - e_{32}\left(\frac{1}{r}\frac{\partial u_n}{\partial r} + \frac{1}{r^2}\frac{\partial u_n}{\partial \theta^2}\right)dA. \tag{33}$$

In the case where $e_{31} = e_{32}$, this integral can be evaluated as

$$e_{31}h\int_{A_{\mathrm{el}}} \frac{k^2\cos(\theta)}{|u_{\max}|}[AJ_1(kr) - CI_1(kr)]dA. \tag{34}$$

The expression for the modal stiffness is quite complex, and instead the modal stiffness is expressed in terms of the modal mass and natural frequency

$$k_m = m_m\omega_n. \tag{35}$$

Now placing (34) into (19) returns an analytic expression for R_m

$$R_m = \frac{\left(\frac{m_m}{m_{\mathrm{tot}}}\right) \pi \lambda_{11}^2 t_{\mathrm{tot}}^2 \sqrt{Y_c \rho_C} |u_{\max}|^2 (12(1-\nu^2))^{-\frac{1}{2}}}{Q_m \left[e_{31} h k^2 \int_{A_{\mathrm{el}}} \cos\theta [A J_1(kr) - C I_1(kr)] r dr d\theta \right]^2} \tag{36}$$

where m_{tot} is the total mass. There are a few things to note. First, not only is R_m is explicitly dependent on υ, but the parameters λ, k, A, C, $|u_{\max}|$, and m_m are all dependent on υ as well. It was empirically determined for various values of υ that $m_m \approx 0.25$ m. Second, although it is not explicit in (36), the in-plane strains are in phase, resulting in a larger value in the integral, and hence enhanced electromechanical coupling [13]. The integral of (36) involves the use of hypergeometric functions, and requires the aid of a computer. Third, R_m expressions for other modes in the DFR family (both disks and annuli) may be derived by using appropriate boundary conditions on (30). Equations for calculating *A, B, C,* and D of (30) are supplied in [30] and [31]. Finally, the motional resistance is predicted to be independent of disk radius. This suggests that resonators with similar performance may be fabricated across a wide range of frequencies.

E. Asymmetric Lamb Modes

The Euler–Bernoulli approximations no longer apply to resonators in which the plate thickness is of the same order of magnitude as the wavelength. These waves are better described by the Rayleigh–Lamb equations. Lamb waves are dispersive and are a superposition of both shear and longitudinal waves. Recent research has targeted the S_0 and SH_0 Lamb modes, with the A_0 mode being considered spurious [32]–[36]. Analytical expression for traveling asymmetric Lamb waves is given in [37]. Standing waves are obtained by superimposing two waves traveling in opposite directions along the x-axis

$$u_x = -(A\xi \sin(\alpha z) - D\beta \sin(\beta z))\sin(\xi x)/|u_{\max}| \tag{37}$$

$$u_z = (A\alpha \cos(\alpha z) + D\xi \cos(\beta z)) \cos(\xi x)/|u_{\max}| \tag{38}$$

where

$$\alpha^2 = \frac{\omega^2}{c_1^2} - \xi^2 \tag{39}$$

$$\beta^2 = \frac{\omega^2}{c_2^2} - \xi^2 \tag{40}$$

and ξ is the wavenumber, and c_1 and c_2 are the longitudinal and shear acoustic velocities, respectively. The ratio of A/D is found via the characteristic equation given in [37]. Dispersion is inherent to the characteristic equation, and therefore, numerical methods must be used to calculate the natural frequency.

In contrast to the previous two modes analyzed, the Lamb waves have a component of strain in the three directions, and consequently, there will be 3-1 shear strain. The implications of the observation will be touched on in this section and more thoroughly discussed in Section II. For PZT and aluminum nitride with the poled axis and electric field in the three directions do not have piezoelectric constants to transduce shear, so (19) becomes

$$\frac{1}{t_p} \int_V e_{31} \frac{du_x}{dx} + e_{33} \frac{du_z}{dz} dV \tag{41}$$

where V is the volume of the piezoelectric layer under the electrode. Equation (19) for the A_0 Lamb mode becomes

$$R_m = \frac{k_m |u_{\max}|^2}{Q_m \omega_n \int_A (e_{31} \overline{f}(z) + e_{33} \overline{g}(z)) \cos(\xi x) dA} \tag{42}$$

$$f(z) = \xi(A\xi \sin(\alpha z) - D\beta \sin(\beta z)) \tag{43}$$

$$g(z) = A\alpha^2 \sin(\alpha z) + D\xi\beta \sin(\beta z) \tag{44}$$

where $\overline{f}$ and $\overline{g}$ are the functions f and g averaged through the thickness of the piezoelectric layer. It is important to reiterate that (42) is only valid for modes with parallel plate electrode topologies in which the fringing field is negligible. Equations (42)–(44) are rather opaque due to the dispersive nature of the mode. The treatment required of dispersion is beyond the scope of this paper, but is treated in [37].

For A_0 modes, mechanical energy is stored in shear, which will increase the modal stiffness. However, energy cannot be directly transduced directly into these strain components. This is undesirable, since the increased stiffness with decreased transduction leads to higher R_m, and decreased k_{eff}^2.

F. Discussion

Equation (19) has been the starting point for each specific R_m. For the simpler case of TBF, a straightforward, easily applied equation was derived. With DFR modes, the added complexity required the use of a computer to solve for mode shape and numerically integrate the transduction integral. Both the TBF and DFR derivations ignored shear stress, under the assumption that for high radius/length to thickness ratios, shear is negligible. Finally, the higher frequency A_0 mode required consideration of dispersion and shear, complicating the analytical mode shape, although a closed-form expression for R is presented.

The problem of the A_0 mode lacking a tractable analytical solution, and more generally, any mode for which there does not exist an applicable analytical solution provides insight into how the methodology of this paper may be capitalized upon. By taking the modal strain and mechanical energy of a general mode (i.e., spurious modes) may be taken directly from FEA and numerically evaluated in the R_m, L_m, C_m, and k_{eff}^2 equations, (15)–(18), this provides designers a method to rapidly predict device performance. This is because the electrical and mechanical *simulation domains* have been decoupled by the use of modal analysis. To clarify, a computationally inefficient Multiphysics simulation is not require; the mechanical domain may be simulated independently and k_{eff}^2 calculated from the obtained information. This has implication for spur design. If the resonator performance parameters for individual modes may be rapidly simulated, then the spur suppression designed may be quickly generated.

The derived equations for R_m and C_m provide nuanced yet important insight into how to identify modes which may have high performance. To understand how, the relationship

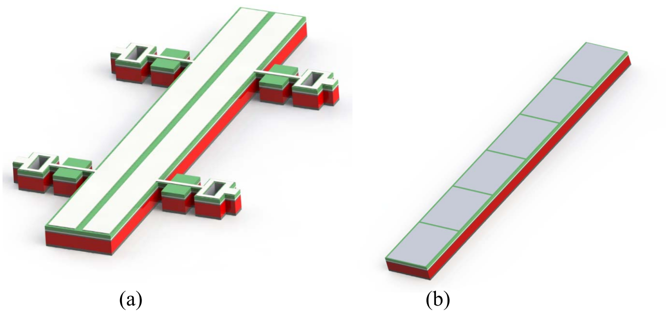
(a) (b)

Fig. 3. Two common electrode patterns used in beam devices. (a) Full-length half-width design. (b) Alternating electrode design.

between the shared integrals of (15) and (19), and the modal stiffness must be considered. The integrals of (15) are a measure of transduction, and a higher value lowers R_m and increases C_m. This agrees with a common observation from piezoelectric MEMS papers that utilizing more than one piezoelectric coefficient often leads to higher performance [13], [38], [39]. Interestingly, shear cannot appear in in the integral of (15) for the materials and topologies these expressions were derived for, even if it physically exists. This is because PZT and aluminum nitride with the poled axis and electric field in the three directions do not have the piezoelectric constants to transduce shear. More generally, any piezoelectric material will have certain strain components it cannot transduce directly. However, when modal stiffness is calculated, all components of stress and strain are represented. If a mechanical mode stores most of the strain energy in strain components which are not directly transduced, the mode will have high motional stiffness, low transduction, and therefore higher R_m and lower C_m, even if it transduces into multiple strain components. From (17), C_m is directly related to the amount of electrical energy transduced into mechanical energy k_{eff}^2. For maximum k_{eff}^2, C_m must be maximized relative to C_0. Therefore, it is not enough that the resonator simply use more than one piezoelectric coefficient to obtain a larger value of the transduction integral for a low R_m and high C_m. A more precise statement is that energy must be directly transduced into and out of strain components, which store a majority of the mechanical energy for minimized R_m and maximized C_m. To this end, computational aide may be enlisted to quickly identify modes with high k_{eff}^2 (independent of Q_m) and potentially low R_m, which is dependent on Q_m.

The mechanical quality factor and loss sources are not directly modeled in this approach to derivation of motional parameters. This is due to the numerous loss mechanisms in parallel manifesting as a single loss factor. These losses include viscous loss [40], anchor loss [41], thermoelastic damping [42], surface losses [43], and fluid damping. These are difficult to separate in measured device and remain an area of active research. For these reasons, the value of Q_m is treated as a problem to be separately modeled.

III. FABRICATION

To validate the derived motional resistance expressions, resonators have been fabricated in a PZT-on silicon-on-insulator (SOI) process [13]. The PZT-on-Silicon fabrication shown in Fig. 4 was performed on a 150-mm-diameter SOI wafer with a 10-μm silicon device layer, 1-μm-thick buried oxide layer, and 650-μm-thick handle layer. To prevent diffusion between the bottom electrode and silicon device layer, a 0.2-μm SiO_2 layer was deposited using plasma enhanced chemical vapor deposition. The bottom electrode, consisting of textured TiO_2 and highly textured (111) Pt, was deposited to a total thickness of 100 nm [44]. (001)-oriented PZT 52/48 is then deposited via chemical solution deposition [45]. Atop this, a 50-nm top electrode consisting of sputter platinum is deposited.

Argon ion milling through the top platinum layer establishes the shape of the electrode. A separate ion mill patterns the PZT and bottom electrode. Then, co-planar waveguides and air bridge contacts to top electrode Pt, consisting of evaporated trilayer of Au/Pt/Cr (730/20/20 nm), were deposited and patterned via liftoff. The resonator body was then defined by a deep reactive ion etch of silicon and reactive ion etch of the buried oxide layer. An atomic layer deposited passivation layer then protects the Si device layer in the subsequent release etch using XeF_2. This passivation layer consisted of 50-nm Al_2O_3 capped with 25-nm HfO_2. This passivation layer is patterned using a CHF_3 reactive ion etch to expose the gold contacts and the handle wafer silicon.

Gold air bridges were then deposited. This air bridge geometry reduces parasitic capacitances by allowing the signal pad to be electrically isolated from the bottom electrode. To construct this, the trench was filled with photoresist to reduce large step heights for subsequent lithography. Then, a second sacrificial photoresist was patterned. It is over this layer which a 2-μm gold air bridge was deposited, then patterned with liftoff. Air bridges were then released using an oxygen plasma etch. Finally, the resonator was released from the handle wafer with an isotropic XeF_2 etch.

IV. EXPERIMENTATION AND VALIDATION

A. Extraction of Experimental Values From S-Parameters

Experimental results are presented for free–free beam flexure devices and disk flexure devices. All scattering (S)-parameter measurements were taken on PM5 RF probe station (Cascade Microtech) at atmospheric pressure. Two-port S-parameters were extracted using a ZVB-8 Rhode & Schwarz vector network analyzer terminated to 50 Ω. Two-port calibration using short, open, load, and through standards was performed on a GGB CSF-5 ceramic substrate. Wide and narrowband measurements were taken. The wideband measurements were used to extract shunt capacitance and tether resistance. The narrowband measurements were used to extract the loaded quality factor as well as motional parameters. As PZT is a ferroelectric piezoelectric, its e constants and permittivity tune nonlinearly with bias voltages. Therefore, each device was tested at various bias voltages to confirm the veracity of the model. This allows more rigorous validation of the models presented here due the ability to test the devices at several operating conditions.

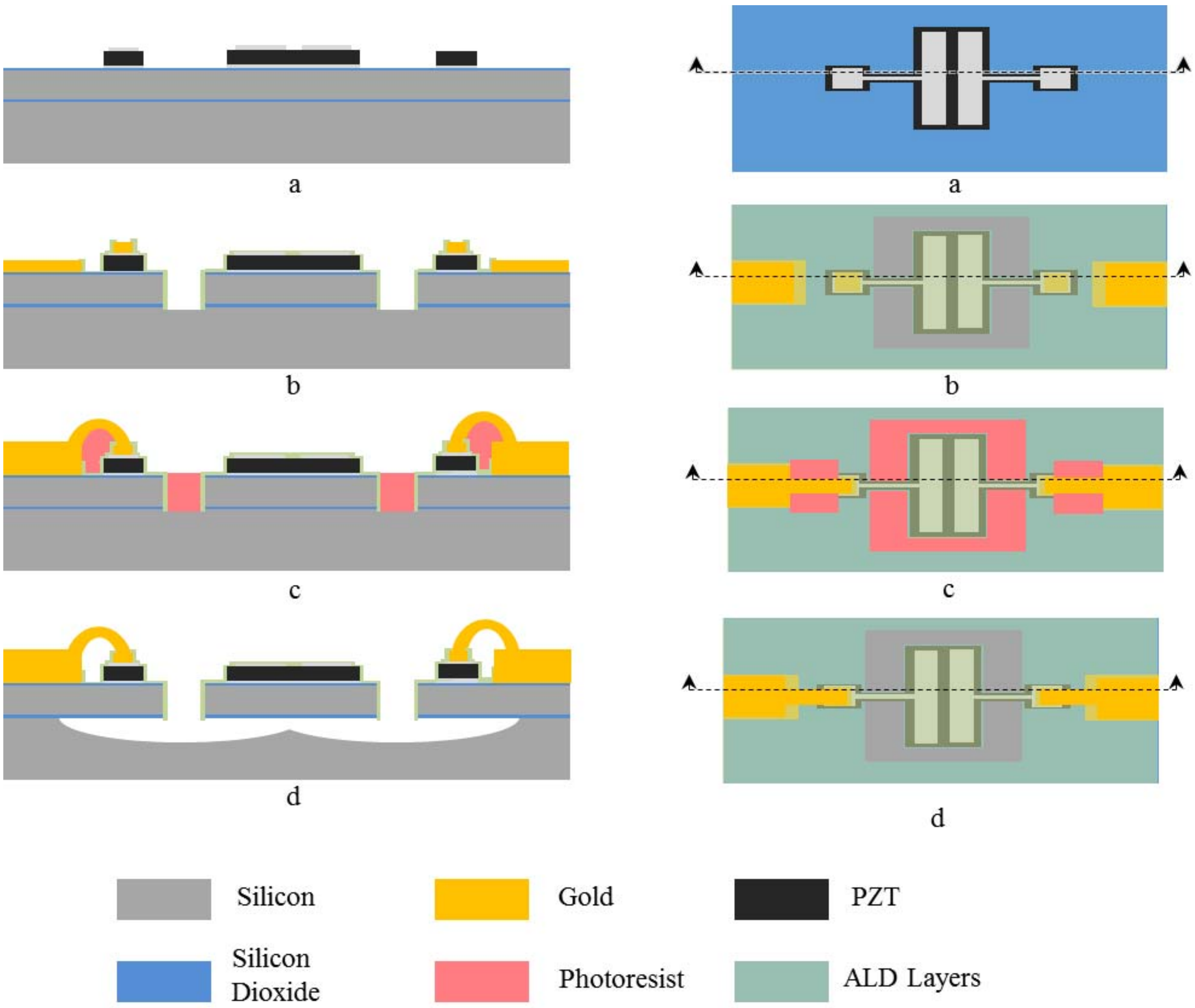

Fig. 4. Process flow for the PZT on silicon process used to fabricate devices in this paper. (a) Material stack after PZT and platinum deposition and patterning. (b) Stack after first-gold deposition, the tenches are etched, and the passivation layer is deposited. (c) Sacrifical photresist is deposited, and the second-gold layer is deposited for air bridges. (d) Sacficial layer is removed, and a XeF_2 release occurs.

B. Parameter Values

The composite moduli and densities appearing in expressions for the modal stiffness and natural frequency were calculated using the rule of mixtures [28]. Values for individual layer moduli and density were independently measured [28], [46]. Lengths, widths, and radii were taken from designed geometries, and layer thicknesses were taken from characterization measurements during fabrication or from nominal thicknesses in the case of the silicon and platinum. Given this, all parameters have been measured, extracted, or taken from modal properties except for Q_m and e_{31}.

Values of e_{31} used in the validation of TBF and DFR modes were arrived at via two distinct methods to more rigorously validate the model. For the first method, e_{31} constants were independently extracted from on-wafer cantilever test structures. Displacement-voltage curves were generated using a Polytech OFV laser Doppler vibrometer system at 90 Hz. From these curves the piezoelectric free strain was extracted. From the strain, an e_{31} was extracted [47].

It is important to note that the test conditions of the resonator and the cantilevers were different. The resonators are operated with a small ac signal superimposed on large dc signal at frequencies above hundreds of kilohertz. The cantilevers were tested with a 90 Hz sine wave with an amplitude of 5 V and a 5-V dc offset. Therefore, frequency dependent effects, such as the degree of polarization, have an impact on piezoelectric coefficients. This is important when considering error between extracted and modeled R_m.

The second method involved a more common approach to validating analytical R_m expressions. The e_{31} values are fit to match the R_m extracted from measurement. If fitted e_{31} values varied in an aphysical or unexpected manner, this would be an indicator of a problem with the model or extraction.

C. Free Disk Results

Six devices were test at 13 dc voltage bias conditions. Fabricated disks had a radius of 56 μm and an electrode shape which may be seen in Fig. 5, along with electrode shape used for analytical evaluation. The electrode shape was designed for optimum excitation via the method of [13]. The targeted

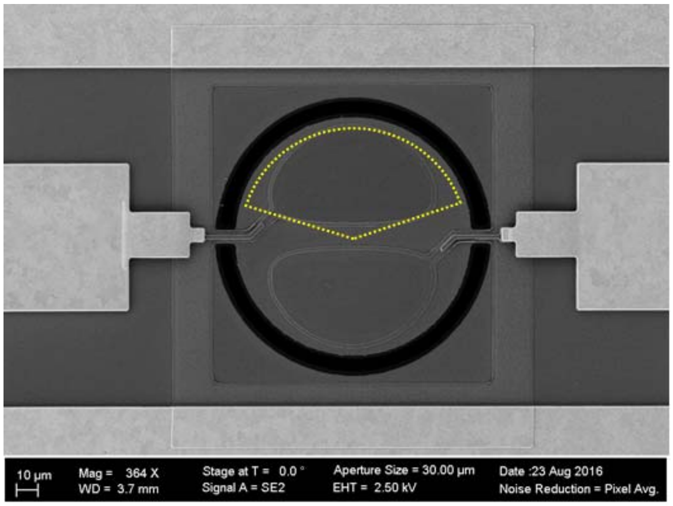

Fig. 5. Image of the fabricated disk resonator taken with a scanning electron microscope. The electrode shape used for analytical validation is superimposed in yellow.

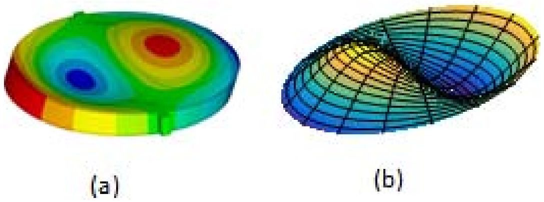

Fig. 6. (a) Mode shape from ANSYS FEA modal analysis. The thin black outline is the true shape of the electrode. (b) Analytical modeshape of the (1,1) disk flexure mode.

(1,1) mode [Fig. 6(a) and (b)] has a nodal diameter, along which the device was anchored. There was good agreement between FEA simulated frequencies and the natural frequencies of fabricated devices. However, there was discrepancy in the predicted analytical natural frequency and measured natural frequency. To ensure the correct mode was analyzed, a Polytec OFV laser Doppler vibrometer was used to ensure the mode being analyzed was the correct mode. Measured frequencies of around 22 MHz were 22%–23% lower than predicted by analytical models. Modal masses calculated from FEA simulations were within 2% of analytical values, so the modal spring was decreased to match analytical and measured frequencies. This subsequently lowers the predicted motional resistance.

As previously stated, the analytical R_m was validated via two methods: by independently extracting e_{31} as well as fitting for agreement between analytical and experimental R_m. For the first method, the error between modeled and extracted motional resistance was 23% across all voltages [Fig. 7(a) and (b)]. There are several possible sources of discrepancy. First, the previously discussed frequency effects from differences in resonator and extraction test conditions are important. Second, shear effects may have an effect, since the model assumes shear to be negligible. Tether effects may add inertia the fabricated resonator, lowering the frequency and raising R_m. For the second method of validation, the e_{31} values ranged from 6 to 11.5, which agrees with the range of values extracted from cantilever test structures.

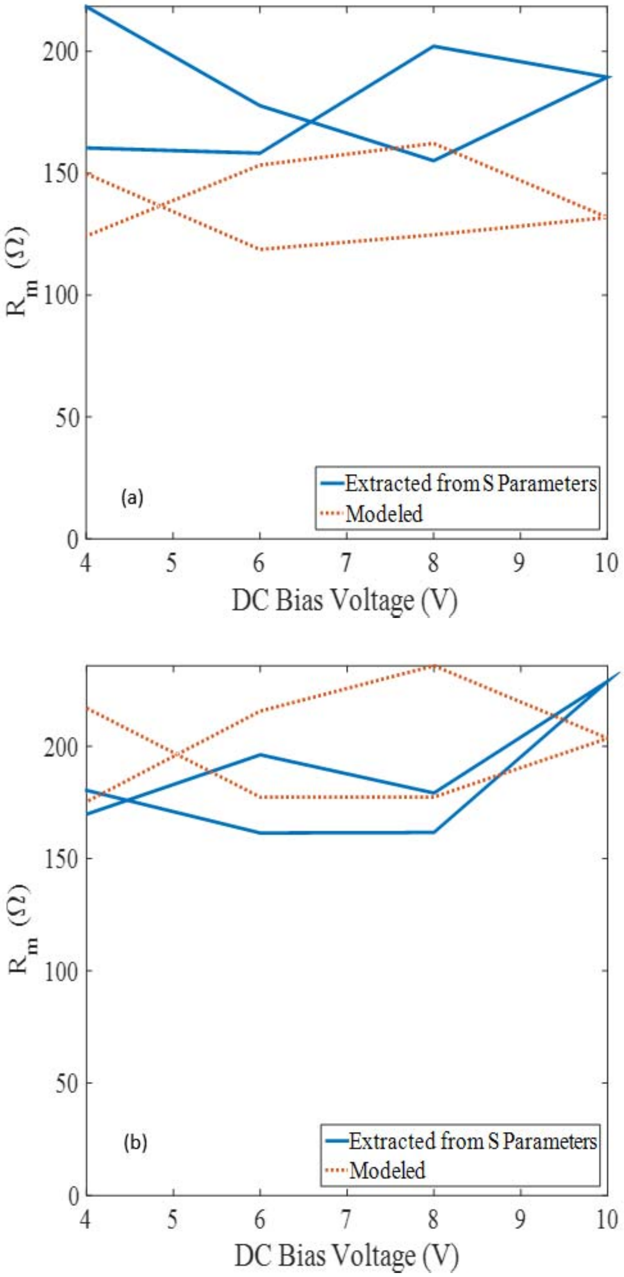

Fig. 7. Example of (a) good and (b) poor agreement between modeled and extracted R_m for the DFRs.

Recently, a −0.92 dB insertion loss resonator was reported consisting of six of the single discs from Fig. 8 in parallel electrically [10]. The device analyzed in Fig. 5(a) was located on the same die as this low-loss resonator. Using the parameters extracted from the single device, its mBVD equivalent circuit was placed in parallel 6 times, simulated, and compared to the S-parameters of the actual device as seen from Fig. 8. The comparison takes place at 8 V and is frequency normalized due to a slight frequency difference between the two resonators. This comparison shows that the models can predict the performance of low-loss resonators as well.

D. Free–Free Transverse Beam Flexure Results

A total of nine devices were tested at 13 bias conditions, and the first harmonic of beam flexure was analyzed (Fig. 9). Each

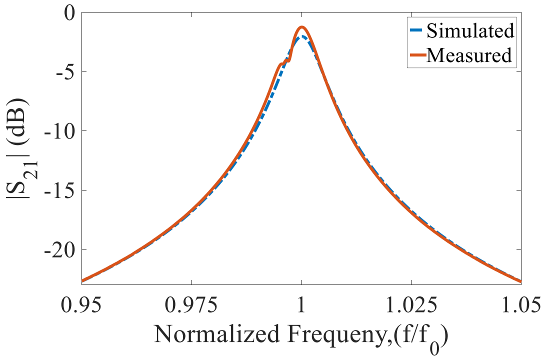

Fig. 8. Comparison of the S-parameters of the model and measurement. The measured data are taken from the −1 dB loss of [12]. The simulated S-parameters predicted by analytically placing six disk resonators in parallel. The Q_m and e_{31} were taken from individual disks and cantilever test structures, respectively, located on the same die as the device from [12].

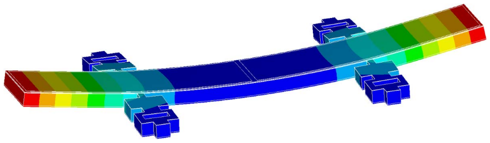

Fig. 9. Mode shape of first harmonic of out-of-plane beam flexure mode from ANSYS simulation.

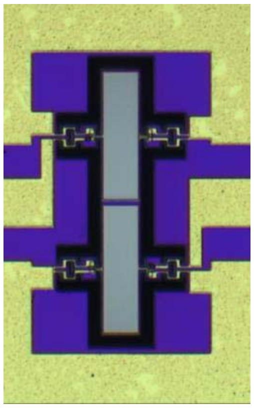

Fig. 10. Micrograph of beam resonator used to verify motional resistance equation.

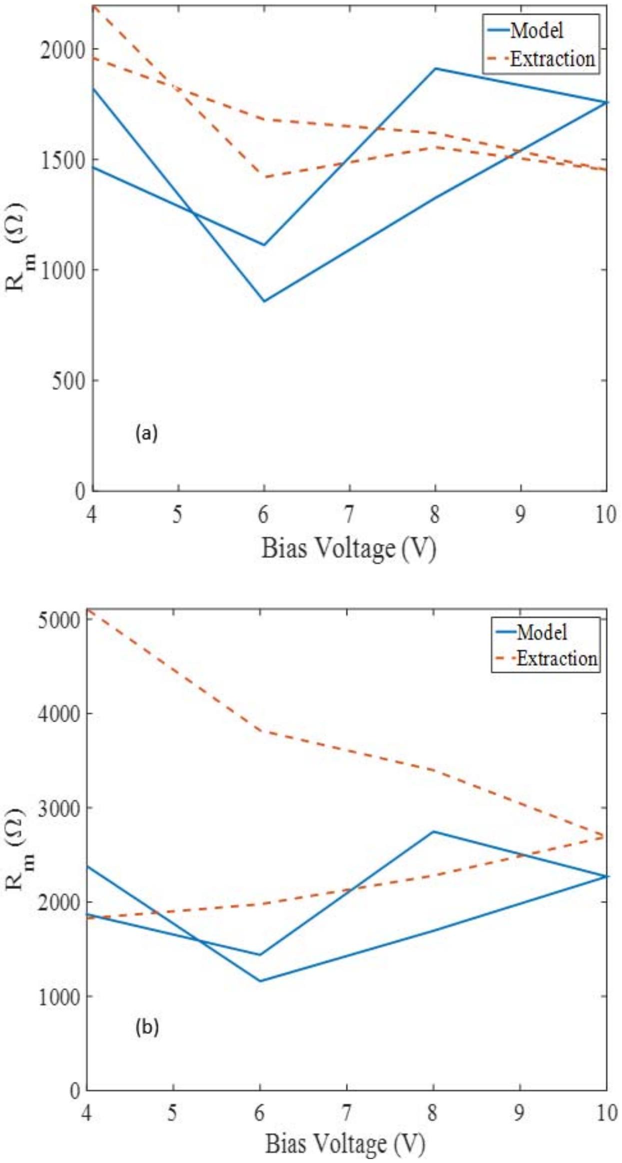

Fig. 11. Example of (a) good and (b) poor agreement between modeled and extracted R_m for the beam flexure resonators.

device located on a different die on the same wafer. Fabricated devices were all 368-μm long with a half-length full-width electrode configuration (Fig. 10). Device widths were varied from 54 to 125 μm. The varied widths affected the shunt impedances and R_m, thereby impacting the resonator loss. These devices were designed for LE, and were anchored at 25% and 75% of the beam length. For the first harmonic of beam flexure, the ideal tether locations are near 27% and 73%. However, the FEA models did not show the tether placement to have a significant effect on the displacement profiles.

Simulated resonator frequencies were compared to measured frequencies with good agreement. In both cases, there was a modest dependence on the width of the resonator. However, analytical natural frequencies from (21) were lower than measured frequencies, which were measured from 650 to 720 kHz, whereas the analytical model predicts frequencies from 636 to 647 kHz. Due to this frequency discrepancy, a scanning Polytech OFV laser Doppler vibrometer system was used to confirm modes were correctly identified as TBF by measuring out-of-plane displacement across the resonator. To find the source of discrepancy between analytical and measured frequencies, the modal mass and modal stiffness were calculated from FEA simulations. Modal masses were found to be within 3% of the analytical value. Therefore, the analytical modal spring value was increased until model and experimental natural frequencies agreed. The analytically calculated stiffnesses were increased significantly, ranging from a 17% to a 42% increase in stiffness due to analytical/measured frequency discrepancies ranging from 8% to 20%. From (19), R_m is directly proportional to modal stiffness, so R_m increased as well.

For validation via the method of extracted e_{31} constants, an example of good agreement and poor agreement may be seen in Fig. 11(a) and (b). For this method, the average error across all devices and voltages was 25%. The sources of error for the beams are expected to be similar to those of the disk.

For the second method of validation, the e_{31} values ranged from 5 to 12, which agrees with range of values extracted from cantilever test structures.

V. CONCLUSION

For the first time, a general analytical expression for the R_m and k_{eff}^2 applicable to any mode of a two-port resonator with parallel plate electrodes modeled by the mBVD has been presented. From this general expression, novel analytical expressions for the motional resistance of TBF, (1,1) DFR and A_0 Lamb wave modes, were derived and with simplifying assumptions. Rigorous R_m model validation was performed using two methods: e_{31} extraction from on-wafer test structures as well as the more common fitting procedure. With this as supporting evidence, if the general expression for current out is adapted properly, it may be utilized to model the mBVD parameters of any piezoelectric resonator.

While the focus on this paper has been analysis of fabricated resonators with analytical mode shapes, there is also opportunity in device design due the rapid and accurate nature of analytical evaluation. In addition, as compared to black box FEA approaches, the expressions that may be derived can provide insights to designers that are more difficult to glean from purely computation methods.

Moreover, the generality of the expressions presented, and the possible speed advantages of this approach should appeal to designers of piezoelectric systems. A filter designer debugging distortion caused by spurious modes could quickly investigate the contribution of individual modes to the frequency response. Oscillator designers could explore novel vibration modes and predict expected coupling. The true displacement of an ultrasonic motor can be predicted as well as the current out of a complicated strain sensing systems. These are a few of the possible benefactors of the work presented in this paper.

Future work will use the general expressions to explore wideband device design for suppressions of spurious modes, as well as validation for other types of modes in other material stacks.

REFERENCES

[1] J. S. Pulskamp, R. Q. Rudy, S. S. Bedair, J. M. Puder, M. G. Breen, and R. G. Polcawich, "Ferroelectric PZT MEMS HF/VHF resonators/filters," in *Proc. IEEE Int. Freq. Control Symp. (IFCS)*, New Orleans, LA, USA, May 2016, pp. 1–4.

[2] G. K. Ho, R. Abdolvand, A. Sivapurapu, S. Humad, and F. Ayazi, "Piezoelectric-on-silicon lateral bulk acoustic wave micromechanical resonators," *J. Microelectromech. Syst.*, vol. 17, no. 2, pp. 512–520, Apr. 2008.

[3] B. Kim, R. H. Olsson, and K. E. Wojciechowski, "AlN microresonator-based filters with multiple bandwidths at low intermediate frequencies," *J. Microelectromech. Syst.*, vol. 22, no. 4, pp. 949–961, Aug. 2013.

[4] G. Piazza, P. J. Stephanou, J. M. Porter, M. B. J. Wijesundara, and A. P. Pisano, "Low motional resistance ring-shaped contour-mode aluminum nitride piezoelectric micromechanical resonators for UHF applications," in *Proc. IEEE Int. Conf. Microelectromech. Syst.*, Miami Beach, FL, USA, Jan./Feb. 2005, pp. 20–23.

[5] D. Horsley, Y. Lu, and O. Rozen, "Flexural piezoelectric resonators," in *Piezoelectric MEMS Resonators*, H. Bhugra and G. Piazza, Eds. Cham, Switzerland: Springer, 2017, ch. 6, pp. 155–170.

[6] J. D. Larson, III, P. D. Bradley, S. Wartenberg, and R. C. Ruby, "Modified butterworth-van dyke circuit for FBAR resonators and automated measurement system," in *Proc. IEEE Int. Ultrason. Symp.*, vol. 1. San Juan, Puerto Rico, Oct. 2000, pp. 863–868.

[7] J. N. Abrams, E. Hanlon, R. G. Sprigg, and D. Macghee, "Multiservice communications for tactial radios in a joint environment," Air, Land, Sea Appl. Center, Tech. Rep. FM 6-02.72, 2002.

[8] *Navy Training System Plan for the AN/ARC-182(V) Radio Set*, document N88-NTSP-A-50-8115DA, 2000.

[9] D. L. DeVoe, "Piezoelectric thin film micromechanical beam resonators," *Sens. Actuators A, Phys.*, vol. 88, no. 3, pp. 263–272, Jan. 2001.

[10] B. Piekarski, D. DeVoe, M. Dubey, R. Kaul, and J. Conrad, "Surface micromachined piezoelectric resonant beam filters," *Sens. Actuators A, Phys.*, vol. 91, no. 3, pp. 313–320, 2000.

[11] A. Prak, M. Elwenspoek, and J. H. J. Fluitman, "Selective mode excitation and detection of micromachined resonators," *J. Microelectromech. Syst.*, vol. 1, no. 4, pp. 179–186, Dec. 1992.

[12] F. D. Bannon, J. R. Clark, and C. T.-C. Nguyen, "High-Q HF microelectromechanical filters," *IEEE J. Solid-State Circuits*, vol. 35, no. 4, pp. 512–526, Apr. 2000.

[13] J. S. Pulskamp *et al.*, "Electrode-shaping for the excitation and detection of permitted arbitrary modes in arbitrary geometries in piezoelectric resonators," *IEEE Trans. Ultrason., Ferroelect., Freq. Control*, vol. 59, no. 5, pp. 1043–1060, May 2012.

[14] R. Q. Rudy, J. S. Pulskamp, S. S. Bedair, J. M. Puder, and R. G. Polcawich, "Piezoelectric disk flexure resonator with 1 dB loss," in *Proc. IEEE Int. Freq. Control Symp. (IFCS)*, New Orleans, LA, USA, May 2016, pp. 1–4.

[15] S. S. Bedair, J. S. Pulskamp, R. G. Polcawich, B. Morgan, J. L. Martin, and B. Power, "Thin-film piezoelectric-on-silicon resonant transformers," *J. Microelectromech. Syst.*, vol. 22, no. 6, pp. 1383–1394, Jun. 2013.

[16] M. Giovannini, S. Yazici, N. K. Kuo, and G. Piazza, "Spurious mode suppression via apodization for 1 GHz AlN contour-mode resonators," in *Proc. IEEE Int. Freq. Control Symp.*, Baltimore, MD, USA, May 2012, pp. 1–5.

[17] R. H. Olsson, K. E. Wojciechowski, and D. W. Branch, "Origins and mitigation of spurious modes in aluminum nitride microresonators," in *Proc. IEEE Int. Ultrason. Symp.*, San Diego, CA, USA, Oct. 2010, pp. 1272–1276.

[18] D. Branch, K. Wojciechowski, and R. Olsson, "Elucidating the origin of spurious modes in aluminum nitride microresonators using a 2-D finite-element model," *IEEE Trans. Ultrason., Ferroelect., Freq. Control*, vol. 61, no. 5, pp. 729–738, May 2014.

[19] A. Gao and S. Gong, "Harnessing mode conversion for spurious mode suppression in AlN laterally vibrating resonators," *J. Microelectromech. Syst.*, vol. 25, no. 3, pp. 450–458, Jun. 2016.

[20] R. Q. Rudy, J. S. Pulskamp, S. S. Bedair, M. G. Breen, J. M. Puder, and R. G. Polcawich, "Low-loss gold-laced PZT-on-silicon resonator with reduced parasitics," in *Proc. IEEE 29th Int. Conf. Micro Electro Mech. Syst. (MEMS)*, Shanghai, China, Jan. 2016, pp. 675–678.

[21] J. He and Z. Fu, *Modal Analysis*, 1st ed. Oxford, U.K.: Heinemann, 2001, p. 107.

[22] N. L. Lobontiu, "Microcantilevers and microbridges: Bending and torsion resonant frequencies," in *Dynamics of Microelectromechanical Systems*, vol. 17, 1st ed. New York, NY, USA: Springer, 2007, pp. 1–5.

[23] L. Meirovitch, "Distributed-parameter systems: Exact solutions," in *Fundamentals of Vibrations*. New York, NY, USA: McGraw-Hill, 2000, ch. 8, sec. 10, p. 440.

[24] *IEEE Standard on Piezoelectricity*, ANSI/IEEE Standard 176-1987, 1988, p. 51.

[25] H. Chandrahalim, S. A. Bhave, R. G. Polcawich, J. Pulskamp, and R. Kaul, "A $Pb(Zr_{0.52}Ti_{0.48})O_3$ transduced fully-differential mechanically coupled frequency-agile filter," *IEEE Electron Device Lett.*, vol. 30, no. 12, pp. 1296–1298, Dec. 2009.

[26] S. S. Bedair *et al.*, "Low loss micromachined lead zirconate titanate, contour mode resonator with 50 Ω termination," in *Proc. IEEE MEMS Conf.*, Paris, France, Jan. 2012, pp. 708–712.

[27] R. D. Blevins, "Straight beams," in *Formulas for Natural Frequency and Mode Shape*. Malabar, FL, USA: Krieger, 1983, pp. 108–109.

[28] R. G. Polcawich and J. S. Pulskamp, "Additive processes for piezoelectric materials: Piezoelectric MEMS," in *MEMS Materials and Processes Handbook*, R. Ghodssi and P. Lin, Eds. Philadelphia, PA, USA: Springer, 2011, pp. 273–353.

[29] H. Chandrahalim *et al.*, "Influence of silicon on quality factor motional impedance and tuning range of PZT-transduced resonators," in *Proc. Solid State Sens., Actuators Microsyst. Workshop*, Hilton Head Island, South Carolina, Jun. 2008, pp. 360–363.

[30] T. B. Gabrielson, "Frequency constants for transverse vibration of annular disks," *J. Acoust. Soc. Amer.*, vol. 105, no. 6, pp. 3311–3317, Jun. 1999.

[31] T. Irvine. (Feb. 2012). *Natural Frequencies of Circular Plate Bending Modes*. [Online]. Available: http://www.vibrationdata.com/circular.pdf

[32] G. Piazza, P. J. Stephanou, J. P. Black, R. M. White, and A. P. Pisano, "Single-chip multiple-frequency RF microresonators based on aluminum nitride contour-mode and FBAR technologies," in *Proc. IEEE Int. Ultrason. Symp. (IUS)*, vol. 2. Sep. 2005, pp. 1187–1190.

[33] R. H. Olsson, III, *et al.*, "A high electromechanical coupling coefficient SH0 Lamb wave lithium niobate micromechanical resonator and a method for fabrication," *Sens. Actuators A, Phys.*, vol. 209, pp. 183–190, Mar. 2014.

[34] R. Wang, S. A. Bhave, and K. Bhattacharjee, "Design and fabrication of S_0 Lamb-wave thin-film lithium niobate micromechanical resonators," *J. Microelectromech. Syst.*, vol. 24, no. 2, pp. 300–308, Apr. 2015.

[35] R. Wang, S. A. Bhave, S. Zhgoon, and K. Bhattacharjee, "Multi-frequency LiNbo3 Lamb wave resonators with $< 3\Omega$ impedance," in *Proc. IEEE Int. Conf. Microelectromech. Syst. (MEMS)*, Shanghai, China, Jan. 2016, pp. 679–682.

[36] S. Gong and G. Piazza, "Design and analysis of lithium–niobate-based high electromechanical coupling RF-MEMS resonators for wide-band filtering," *IEEE Trans. Microw. Theory Techn.*, vol. 61, no. 1, pp. 403–414, Dec. 2012.

[37] K. F. Graff, "Wave propagation in rods and plates," in *Wave Motion in Elastic Solids*. New York, NY, USA: Dover, 1975, pp. 440–450.

[38] J. M. Puder, S. S. Bedair, J. S. Pulskamp, R. Q. Rudy, R. G. Polcawich, and S. A. Bhave, "Higher dimensional flexure mode for enhanced effective electromechanical coupling in PZT-on-silicon MEMS resonators," in *Proc. IEEE Int. Conf. Sens., Acuators, Microsyst. (TRANSDUCERS)*, Anchorage, AK, USA, Jun. 2015, pp. 2017–2020.

[39] C. Cassella, Y. Hui, Z. Qian, G. Hummel, and M. Rinaldi, "Aluminum nitride cross-sectional Lamé mode resonators," *J. Microelectromech. Syst.*, vol. 25, no. 2, pp. 275–285, 2016.

[40] C. E. Reed, K. K. Kanazawa, and J. H. Kaufman, "Physical description of a viscoelastically loaded AT-cut quartz resonator," *J. Appl. Phys.*, vol. 68, no. 5, pp. 1993–2001, Sep. 1990.

[41] B. P. Harrington and R. Abdolvand, "In-plane acoustic reflectors for reducing effective anchor loss in lateral–extensional MEMS resonators," *J. Micromech. Microeng.*, vol. 21, no. 8, p. 085021, Jul. 2011.

[42] R. Lifshitz and M. L. Roukes, "Thermoelastic damping in micro- and nanomechanical systems," *Phys. Rev. B, Condens. Matter*, vol. 61, no. 8, p. 5600, Feb. 2000.

[43] K. L. Ekinci and M. L. Roukes, "Nanoelectromechanical systems," *Rev. Sci. Instrum.*, vol. 76, no. 6, p. 061101, Apr. 2005.

[44] D. M. Potrepka, G. R. Fox, L. M. Sanchez, and R. G. Polcawich, "Pt/TiO_2 rowth templates for enhanced PZT films and MEMS devices," in *Proc. Mater. Res. Soc. Online Library*, vol. 1299. 2010.

[45] L. M. Sanchez, D. M. Potrepka, G. R. Fox, I. Takeuchi, and R. G. Polcawich, "Improving PZT thin film texture through Pt metallization and seed layers," in *Proc. Mater. Res. Soc. Online Library*, vol. 1299. Jan. 2010.

[46] S. Yagnamurthy, I. Chasiotis, J. Lambros, R. G. Polcawich, J. S. Pulskamp, and M. Dubey, "Mechanical and ferroelectric behavior of PZT-based thin films," *J. Microelectromech. Syst.*, vol. 20, no. 6, pp. 1250–1258, 2011.

[47] J. M. Puder *et al.*, "Modeling of high electric bias field induved piezoelectric nonlinearity," presented at the Int. Workshop Acoust. Trans. Mater. Devices, Jun. 2016.

Jonathan M. Puder (S'17–M'17) received the B.S. and M.S. degrees in mechanical engineering from Cornell University, Ithaca, NY, USA, in 2012 and 2016, respectively, where he is currently pursuing the Ph.D. degree in mechanical engineering.

He joined the OxideMEMS Group, Cornell University, as an Undergraduate Research Assistant in 2012, where he continues as a Graduate Research Assistant. He is also a Mechanical Engineer with the PiezoMEMS Group, U.S. Army Research Laboratory, Adelphi, MD, USA, where he has been since 2014. His current research interests include piezoelectric MEMS resonance-based devices.

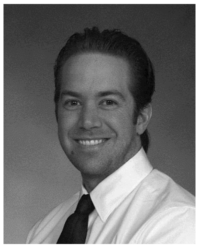

Jeffrey S. Pulskamp received the B.S. degree in mechanical engineering from the University of Maryland at College Park, College Park, MD, USA, in 2000.

He is a MEMS Design and Mechanical Engineer with the Micro and Nano Materials and Devices Branch, U.S. Army Research Laboratory, Adelphi, MD, USA. His current research interests include RF MEMS resonators and switches, electro-mechanical design and modeling of MEMS, and millimeter-scale robotics. He has authored two book chapters on the design and fabrication of piezoelectric MEMS devices. He currently holds ten patents related to piezoelectric MEMS devices and has an additional five patents pending.

Ryan Q. Rudy received the B.S.E. and M.S.E. degrees in mechanical engineering from the University of Michigan, Ann Arbor, MI, USA, in 2009 and 2010, respectively, and the Ph.D. degree in mechanical engineering from the University of Maryland at College Park, College Park, MD, USA, in 2014, with a focus on miniaturized ultrasonic motors.

He is a Mechanical Engineer with the Micro and Nano Materials and Devices Branch, U.S. Army Research Laboratory, Adelphi, MD, USA. His current research interests include piezoelectric MEMS, specifically piezoelectric electromechanical resonators and filters.

Ronald G. Polcawich (M'07–SM'16) received the B.S. degree in materials science and engineering from Carnegie Mellon University, Pittsburgh, PA, USA, in 1997, and the M.S. degree in materials and the Ph.D. degree in materials science and engineering from Penn State University, State College, PA, USA, in 1999 and 2007, respectively.

He is a Staff Researcher with the Micro and Nano Materials and Devices Branch, U.S. Army Research Laboratory (ARL), Adelphi, MD, USA. He is currently the Team Lead for PiezoMEMS Technology, ARL, with a focus on developing component technologies to enable cognitive RF communication and radar systems and MEMS inertial and aiding sensors to provide position, navigation, and timing solutions for SWAP-C constrained platforms. He currently holds 13 patents, has ten patent applications pending review. He has authored over 70 articles and three book chapters on fabrication and design of piezoelectric MEMS devices using lead zirconate titanate (PZT) thin films. His current research interests include materials processing of PZT thin films, MEMS fabrication, RF components, MEMS actuator technologies, mm-scale robotics, MEMS inertial sensors, and sensors for aiding inertial systems.

Dr. Polcawich is a member of the IEEE Ferroelectrics Committee and Technical Program Committee IV Applications of Ferroelectrics. He served as an elected member of the IEEE Ultrasonics, Ferroelectrics, and Frequency Control (UFFC) Administrative Committee from 2014 to 2016. He has been the Chair of the UFFC Membership Committee since 2016. He received the 2012 Presidential Early Career Award for Scientists and Engineers and the 2015 IEEE UFFC Ferroelectrics Young Investigator Award. He is on the Technical Advisory Committee for the PiezoMEMS Workshop, co-organized the 2013 meeting at Washington, DC, USA, and a Co-Organizer for the 2018 meeting at Orlando, FL, USA.

Sunil A. Bhave (S'99–M'05–SM'10) received the B.S. and Ph.D. degrees in electrical engineering and computer science from the University of California at Berkeley, Berkeley, CA, USA, in 1998 and 2004, respectively.

He was with Cornell University, Ithaca, NY, USA, where he was an Associate Professor with the School of Electrical and Computer Engineering for ten years. In 2015, he joined the Department of Electrical and Computer Engineering, Purdue University, West Lafayette, IN, USA, as an Associate Professor. His current research interests include exploring, understanding, and exploiting interdomain coupling in optomechanical, spin-acoustic, and atom-MEMS systems to design inertial sensors, clocks, and field-programmable microwave chipsets.

Dr. Bhave was a recipient of the National Science Foundation Early CAREER Development Award in 2007, the Defense Advanced Research Projects Agency Young Faculty Award in 2008, and the IEEE Ultrasonics Young Investigator Award in 2014. Along with his students, he received the Roger A. Hakan Best Paper Award at the International Electron Devices Meeting in 2007, and the Student Paper Competition Award at the IEEE International Ultrasonics Symposium in 2009 and the IEEE Photonics Conference in 2012.